The Astrophysical Journal
Preprint typeset using LaTeX style emulateapj v. 5/2/11

arXiv:1606.08845v1 [astro-ph.SR] 28 Jun 2016

INSIGHTS FROM SYNTHETIC STAR-FORMING REGIONS: III. CALIBRATION OF MEASUREMENT TECHNIQUES OF STAR-FORMATION RATES

Christine M. Koepferl[1,2], Thomas P. Robitaille[1,3], and James E. Dale[4]
[1] Max Planck Institute for Astronomy, Königstuhl 17, D-69117 Heidelberg, Germany
[2] Scottish Universities Physics Alliance (SUPA), School of Physics and Astronomy, University of St Andrews North Haugh, St Andrews, KY16 9SS, UK
[3] Freelance Consultant, Headingley Enterprise and Arts Centre, Bennett Road Headingley, Leeds LS6 3HN
[4] University Observatory Munich, Scheinerstr. 1, D-81679 Munich, Germany
(Received 29 January 2016; Accepted 8 March 2016)
The Astrophysical Journal

ABSTRACT

Through an extensive set of realistic synthetic observations (produced in Paper I), we assess in this part of the paper series (Paper III) how the choice of observational techniques affects the measurement of star-formation rates (SFRs) in star-forming regions. We test the accuracy of commonly used techniques and construct new methods to extract the SFR, so that these findings can be applied to measure the SFR in real regions throughout the Milky Way. We investigate diffuse infrared SFR tracers such as those using 24 µm, 70 µm and total infrared emission, which have been previously calibrated for global galaxy scales. We set up a toy model of a galaxy and show that the infrared emission is consistent with the intrinsic SFR using extra-galactic calibrated laws (although the consistency does not prove their reliability). For local scales, we show that these techniques produce completely unreliable results for single star-forming regions, which are governed by different characteristic timescales. We show how calibration of these techniques can be improved for single star-forming regions by adjusting the characteristic timescale and the scaling factor and give suggestions of new calibrations of the diffuse star-formation tracers. We show that star-forming regions that are dominated by high-mass stellar feedback experience a rapid drop in infrared emission once high-mass stellar feedback is turned on, which implies different characteristic timescales. Moreover, we explore the measured SFRs calculated directly from the observed young stellar population. We find that the measured point sources follow the evolutionary pace of star formation more directly than diffuse star-formation tracers.

1. INTRODUCTION

In a star-forming region, gas is transformed into stars. While the dominating driving mechanisms and the impact of the different stellar feedback mechanisms are still debated in the field, there are different approaches among researchers to address these questions: In the observational approach, the characteristic observable properties of star-forming regions are used to study and compare different regions in an attempt to disentangle the dominant driving mechanisms of star formation. In the theoretical approach, (magneto-)hydrodynamical simulations (e. g. SPH: smoothed particle hydrodynamics) study the formation processes of star-forming regions. However, in state-of-the-art simulations of star-forming regions the total SFR is always too high and some simulations fail to reproduce the correct distribution of stellar masses when comparing with observations (c. f. Krumholz et al. 2012, Krumholz et al. 2011, Urban et al. 2010, Bate 2009 and also Dale & Bonnell 2011; Dale et al. 2012, 2013a,b, 2014, referred to as D14 SPH simulations). Different implementations of stellar feedback, such as ionization and winds, help to suppress star formation and the accretion mechanism, however, these mechanisms do not restrain star formation enough (c. f. Bate 2014, Federrath et al. 2014, Hansen et al. 2012, and also D14 SPH simulations). For more detail about high-mass stellar feedback and its implementation, see the review of Dale (2015).

cmk8@st-andrews.ac.uk

The measured star-formation properties are the observational benchmark between reality and theory. Examples of properties include the total gas mass $M_{\rm gas}$ and the total stellar mass M_* in a star-forming region (as summarized by Dale et al. 2014). The property which connects stellar mass and total gas mass is the efficiency of the transition from gas to stars and can be expressed by the star-formation efficiency (SFE) at a certain time t:

$$\mathrm{SFE}(t) = \frac{M_*(t)}{M_*(t) + M_{\rm gas}(t)}. \quad (1)$$

Another important physical property defining a star-forming region is the rate at which it forms stars. The average SFR between times t_0 and t is defined as:

$$\mathrm{SFR}(t) = \frac{M_*(t) - M_*(t_0)}{t - t_0} = \frac{M_*(t) - M_*(t_0)}{\delta t_*}, \quad (2)$$

where $\delta t_* = t - t_0$ is the characteristic timescale over which the SFR is measured. There exists a large variety of tracers to measure the SFR. Each technique probes star formation within a certain characteristic timescale δt_*, which varies from tracer to tracer. One can divide the different techniques into two categories:

1. **Indirect Techniques**
   Young high-mass stars ionize the material around them with X-ray and ultra-violet (UV) radiation. This process can be used to trace star formation in

different wavelength regimes, since the ionized electrons emit free-free centimeter continuum, while ionized hydrogen emits Hα radiation in a bubble around the young ionizing stars. The ionization strength is correlated with the mass of the ionizing objects (e. g. Panagia 1973). Moreover, young high-mass objects also emit weaker UV radiation which is then absorbed by the surrounding dust and produces diffuse infrared emission. However, in this picture, the thermal emission of young low-mass stars is neglected. Consequently, these methods, which make use of the free-free, Hα and diffuse infrared emission (originating from UV), are indirect methods, since they do not trace the actual young stars but the effect of the high-mass young stars on their surrounding dust and gas. Since these indirect techniques only trace the high-mass stars, the findings need to be extrapolated to the total stellar population by assuming an initial mass function (IMF). For more details on indirect tracers, see the review of Kennicutt & Evans (2012) and Calzetti (2013).

2. **Direct Techniques**
Direct star-formation tracers trace the sites of young stars directly. Young stellar objects (YSOs) heat the surrounding dust which then emits in the infrared. In the circumstellar material, the dominating 24 µm emission originates closer to the star than the 70 µm emission. The 24 µm emission can act as a good tracer since the resolution is currently better than for far-infrared (FIR) emission. Moreover, the 24 µm emission is unrelated to the large scale infrared emission from hydrodynamical temperature fluctuations when comparing to the FIR emission which is background dominated (Koepferl et al. 2016a, referred to as Paper II). However, selecting a sample of young objects is not a trivial task, as shown by Koepferl et al. (2015) for the central molecular zone (CMZ).

The measurement of star-formation tracers, such as the SFR, requires different approaches for different astronomical objects, such as galaxies, giant molecular clouds or single star-forming regions:

1. **Extra-galactic Scales**
For distant galaxies, individual counting of forming stars is not possible, since not even single star-forming regions are resolved. The measured properties of star formation are therefore averaged over large scales. Hence, indirect, atomic, recombination line tracers (e. g. Hα) or indirect diffuse tracers (e. g. 24 µm, 70 µm, total infrared) are commonly used in the extra-galactic community. Those indirect methods have been calibrated using galaxy model spectra, such as STARBURST99 (Leitherer et al. 1999), and are constantly improved empirically (e. g. Murphy et al. 2011; Calzetti et al. 2010; Rieke et al. 2009; Pannella et al. 2015; Leroy et al. 2013, 2012; Wuyts et al. 2011; Leroy et al. 2008).

2. **Local Galactic Scales**
For local regions within the Milky Way, the SFR can be directly evaluated through proto-stellar counting. Using young stars directly has the clear advantage that the sites of star formation are counted and not the total emission which is produced by star formation or other processes. For example, Evans et al. (2009) estimated the SFR for regions in the Milky Way through directly counting YSOs in the mid-infrared (MIR) (from the Cores to Disks Legacy (c2d) project) down to low-mass objects. For their complete sample, they assumed an average mass of $0.5\,M_\odot$ and a characteristic timescale of $\delta t_* = 2\,\mathrm{Myr}$. Robitaille & Whitney (2010) estimated the SFR of the Milky Way by directly counting YSOs emitting in the infrared (Galactic Legacy Infrared Mid-Plane Survey Extraordinaire, GLIMPSE), using a population synthesis model to extrapolate the number of sources below the detection limit. In addition, indirect tracers, such as free-free emission, have been applied for sub-regions of the Milky Way. For example, Longmore et al. (2013) measured the SFR of the CMZ using free-free emission. Diffuse infrared tracers (e. g. 24 µm, 70 µm, total infrared) have also been used for the Milky Way and single star-forming regions therein (Barnes et al. in preparation; Crocker et al. 2011; Yusef-Zadeh et al. 2009; Misiriotis et al. 2006). However, indirect tracers have not yet been critically tested for the Milky Way.

3. **Intermediate Scales**
Keeping in mind that indirect methods have not yet been calibrated for regions within the Milky Way, it is challenging to measure the SFR for regions across the Galactic plane where the detection of point sources is limited. One of the major flaws of the star-formation tracers is that they have been calibrated from far-to-near. However, with better infrared observations (Galactic and extra-galactic) at hand and state-of-the-art radiative transfer codes, we now have the opportunity to improve the relation between the star-formation tracers and the SFR from the bottom up. Once reliable direct techniques to estimate the star-formation properties have been calibrated at local scales, they can be used to calibrate indirect techniques for local regions, which then also can be used for regions across the Galaxy and for distant galaxies.

When calibrating different techniques to infer star-formation properties, the discussion of the timescales δt_* is an essential ingredient. Note that different techniques, which make use of different physical processes that act on different timescales δt_*, produce different SFRs for the same region if the intrinsic rate is not constant over time. On small scales, the SFR is not necessarily expected to be constant. On the other hand, on the scale of the Galaxy, the rate of star formation is expected to be approximately constant on $\sim 100\,\mathrm{Myr}$ timescales and hence the different techniques should produce comparable rates. For example, Chomiuk & Povich (2011) showed that the measured SFR values for the Milky Way (e. g. Robitaille & Whitney 2010; Murray & Rahman 2010; Misiriotis et al. 2006) agreed when scaling by timescale to a value of $(1.9 \pm 0.4)\,M_\odot\,\mathrm{yr}^{-1}$.

1.1. *Motivation*

Since the observable star-formation properties are used to test theoretical simulations, which might then help us to understand the main driving mechanisms of star formation, it is essential that the measurements of these properties are as accurate as possible. In this work, we test the accuracy and calibrate relations between star-formation tracers and physical properties, such as the total gas mass $M_{\rm gas}$, the SFR and the total stellar mass M_*, using indirect and direct techniques. In Koepferl et al. (2016a), referred to as Paper II, we tested the accuracy of measurements of the total gas mass. In this part of the series, referred to as Paper III, we will focus on techniques that make use of dust tracers to infer star-formation rates, using the set of realistic synthetic observations developed in Koepferl et al. (2016c) referred to as Paper I.

1.2. *Recapitulation*

In the following we will briefly summarize Paper I, where we produced synthetic observations of multiple time-steps of a simulated star-forming region. We used the D14 SPH simulations (Dale & Bonnell 2011; Dale et al. 2012, 2013a,b, 2014) of a 30 pc wide synthetic star-forming region with different high-mass stellar feedback mechanisms implemented (*run I*: stellar ionization and winds). The configurations of the simulated star-forming from the D14 SPH simulations are described in more detail in Paper I and D14.

We extend the SPH simulations by post-processing the simulation output through radiative transfer calculations. We account for the stellar heating of the dust using HYPERION, a 3-d dust continuum Monte-Carlo radiative transfer code. For more details about HYPERION and radiative transfer in general, see Robitaille (2011) and Steinacker et al. (2013).

In Paper I, we presented a mass conserving algorithm which converts an SPH particle distributions (e. g. density) to a Voronoi tessellation used by the radiative transfer code. In order to better recover the MIR flux, we refined the density structure close to YSOs to overcome the resolution limit of the SPH simulation. We tested different extrapolation techniques for the refinement: rotationally flattened (Ulrich 1976) envelope profile and a power-law envelope profile. In order to improve the computational efficiency, we precomputed with the radiative transfer code analytical models of YSOs within 500 AU of every accreting proto-star. The typical dust-to-gas ratio of $\frac{\rm dust}{\rm gas} = 0.01$ (Draine 2011) was used for the radiative transfer calculations together with the Draine & Li (2007) polycyclic aromatic hydrocarbon (PAH) dust grains description. Moreover, we combined the calculated radiative transfer dust temperature with an ambient background temperature typical for the relatively cloudless regions in the Galactic plane ($T_{\rm iso} = 18$ K, see also Paper II). For more information about the radiative transfer set-up of synthetic star-forming regions, see Paper I.

We used the FLUXCOMPENSATOR to produce realistic synthetic observations for all the radiative transfer images, by accounting for the extinction, the transmission curves of the telescope and detector, the pixel-size and the point-spread-function (PSF) convolution. We combined these realistic synthetic observations with a relatively empty patch of the Galactic plane (see also Paper II) resulting in synthetic observations which are directly comparable to real observations. For more information about the FLUXCOMPENSATOR, see Koepferl & Robitaille, in preparation, referred to as Paper FluxCompensator. We present the produced $\sim$5800 realistic synthetic observations in the online material of Paper I resulting from combinations of the following configurations:

- **23 Time-steps**
  We select 23 equally spaced time-steps (step width: $\Delta t = 149\,000$ yr) over 3.3 Myr from the SPH simulations between the formation of the first proto-star and the first supernova. Once three high-mass stellar particles above 20 $M_\odot$ have formed ($\sim$1.7 Myr) the ionization and winds of high-mass stars are switched on.

- **3 Circumstellar Set-ups**
  We explored three different circumstellar refinement scenarios: as a control run one without added envelopes (CM1) and two envelope refinements beyond the resolution limit of the simulation. In the two other cases we used pre-computed analytical models of a circumstellar disk together with a rotationally flattened envelope (CM2, Ulrich 1976) and a power-law envelope (CM3) profile.

- **3 Orientations**
  We constructed synthetic observations for three perpendicular viewing angles: xy plane (O1), xz plane (O2) and yz plane (O3).

- **2 Distances**
  We pushed the synthetic observations to two different distances: 3 kpc (D1) and 10 kpc (D2). We chose this distances in order to be comparable to nearby high-mass star-forming regions, such as Carina, Westerhout 4,5 and the Eagle Nebula and more distant regions across the Galactic plane. Using a built-in function of the FLUXCOMPENSATOR, we calculate the interstellar extinction (Kim et al. 1994) with $A_V = 10$ and $A_V = 20$ for the two different distances, respectively.

- **7 Bands**
  We produced realistic synthetic observations in the following bands with the respective appropriate transmission curve, PSF and pixel-size (listed in brackets): Infrared Array Camera (IRAC) 8 µm (1.″2), Multiband Imaging Photometer for *Spitzer* (MIPS) 24 µm (2.″4), Photoconductor Array Camera and Spectrometer (PACS) 70 µm (3.″2), PACS 160 µm (4.″5), Spectral and Photometric Imaging Receiver (SPIRE) 250 µm (6.″0), SPIRE 350 µm (8.″0) and SPIRE 500 µm (11.″5).

- **2 Backgrounds**
  We analyze every realistic synthetic observations and also a respective counterpart combined with a realistic background.

For more information about the derivation of realistic synthetic observations, see Paper I and Paper FluxCompensator.

1.3. *Outline*

With these realistic synthetic observations, which are directly comparable to real observations, we can start our analysis of star-formation dust tracers. The reliability of three different diffuse star-formation dust tracers will be explored on local scales in Section 2. In Section 3 we calibrate these relations with different characteristic timescales and we set constrains for these star-formation tracers on global scales. We provide a new indirect relation between the luminosity and the stellar mass in Section 4. In Section 5, we present insights of the protostellar counting of our synthetic point sources. In Section 6, we discuss the biases of star-formation properties before we summarize in Section 7. In a follow-up paper (Koepferl et al., in preparation, referred to as Paper IV), we will present a detailed parameter study of our synthetic point-source catalogues and the resulting SFR.

2. DIFFUSE STAR-FORMATION TRACERS

There exist a variety of indirect diffuse infrared SFR tracers which use the total flux in certain bands to derive the SFR. For a detailed review, see Kennicutt & Evans (2012) or Calzetti (2013) or Section 1. These techniques, which use tracers in the infrared continuum, rely on the assumption that young high-mass stars emit strongly at UV wavelengths, which is then completely absorbed by the dust, and then completely re-emitted in the infrared. Diffuse infrared star-formation tracers assume further that the flux originates from all high-mass stars formed since a certain timescale δt_*. The shortcoming here is that the radiation of the majority of smaller stars is neglected.

The diffuse techniques use the total flux in a certain observed band with wavelength λ. The conversion from total flux, hence total luminosity $\nu L_\nu(\lambda)$, to SFR always follows the same pattern (see Kennicutt & Evans 2012):

$$\frac{\mathrm{SFR}_\lambda}{M_\odot\,\mathrm{yr}^{-1}} = a\left(\frac{\nu L_\nu(\lambda)}{\mathrm{ergs\,s}^{-1}}\right)^b \tag{3}$$

In order to get the total luminosity $\nu L_\nu(\lambda)$ in a certain band (e. g. MIPS 24 µm), we calculate the total flux $\nu F_\nu(\lambda)$ of the respective realistic synthetic observations. For this and upcoming photometric calculations in this paper, we use the FluxCompensator; for a more detailed description, see Paper FluxCompensator. Following Paper II, we correct for the background emission and deredden with the same optical extinction A_V as before. The resulting corrected total flux $\nu F_\nu^{\mathrm{corr}}(\lambda)$ is in units of $\mathrm{ergs\,s}^{-1}\,\mathrm{cm}^{-2}$. In the respective band, the total luminosity can then be estimated with the measured distance D, where we assume again the correct distance, as in Paper II and set in Paper I.

$$\nu L_\nu(\lambda) = 4\pi D^2 \nu F_\nu^{\mathrm{corr}}(\lambda) \tag{4}$$

While there are many relations to infer the SFR from diffuse tracers, in what follows, we will limit ourselves to only test the accuracy of the techniques[1] using dust tracers, which have been summarized in the review of Kennicutt & Evans (2012) and are commonly used in the community (e. g. Barnes et al. in preparation; Crocker et al. 2011; Yusef-Zadeh et al. 2009). Note that these techniques have been developed by and for the extra-galactic community, hence for entire galaxies, and assume characteristic timescales of $\delta t_* = 100\,\mathrm{Myr}$ (Kennicutt & Evans 2012; Murphy et al. 2011; Calzetti et al. 2010; Rieke et al. 2009). These techniques have not yet been tested sufficiently for (smaller, local) individual regions. Therefore, we analyze the reliability of these techniques in this section.

In Figure 1, we plot the intrinsic instantaneous SFR directly from the simulation (red solid curve), which we call $\mathrm{SFR}_{\mathrm{sim}}(\delta t_* = \Delta t)$ from now on, since it was calculated with the star-formation timescale δt_* equal to the time-step of the simulation Δt. To compare it to the measured techniques, which follow characteristic timescales of $\delta t_* = 100\,\mathrm{Myr}$, we convolve (see Press et al. 1992) $\mathrm{SFR}_{\mathrm{sim}}(\delta t_* = \Delta t)$ with a normalized top-hat function (see Bronstein et al. 2005) of width $100\,\mathrm{Myr}$[2]. The resulting convolved function (red dashed curve), hereafter called $\hat{\mathrm{SFR}}_{\mathrm{sim}}(\delta t_* = 100\,\mathrm{Myr})$, is around three orders of magnitude lower since $\Delta t/\delta t_* = 149\,000\,\mathrm{yr}/100\,\mathrm{Myr} \approx 10^{-3}$.

2.1. *Method SFR24 — 24 µm Tracer*

Rieke et al. (2009) empirically calibrated a SFR-to-luminosity relation of 24 µm emission:

$$\frac{\mathrm{SFR}_{24\,\mu\mathrm{m}}(\delta t_* = 100\,\mathrm{Myr})}{M_\odot\,\mathrm{yr}^{-1}} = 2.03\times10^{-43}\times \times\frac{\nu L_\nu(24\,\mu\mathrm{m})}{\mathrm{ergs\,s}^{-1}}, \tag{5}$$

which they found to be valid within $2.3\times10^{42}\,\mathrm{ergs\,s}^{-1} \leq \nu L_\nu(24\,\mu\mathrm{m}) \leq 5.0\times10^{43}\,\mathrm{ergs\,s}^{-1}$. Nevertheless, we will use this technique for synthetic observations with a total flux less than $10^{40}\,\mathrm{ergs\,s}^{-1}$ to test whether the SFR24 technique can be used for single star-forming regions.

Using Eq. 5, we derive the $\mathrm{SFR}_{24\,\mu\mathrm{m}}(\delta t_* = 100\,\mathrm{Myr})$ for our set of synthetic observations in MIPS 24 µm for every time-step. We present the results when combining with a background (black dots) and without background (black stars) in Figure 1. Note that we averaged all values of different orientations, distances and circumstellar set-ups to one value per time-step because the total flux is very similar between all cases. We highlight the deviation, which is due to optically thick regions for different orientations and slight flux deviations, due to the different circumstellar set-ups, by black error-bars.

In Figure 1 (left panel), we can see that the SFR24 technique produces similar results for the measurements of the synthetic observations with a combined background (black dots) and without a background (black stars). The fact that the $\mathrm{SFR}_{24\,\mu\mathrm{m}}(\delta t_* = 100\,\mathrm{Myr})$ for the models including the background is higher is likely due to an incomplete subtraction of the non-uniform background. Nevertheless, the measured values are up to three orders of magnitude higher than the rate

[1] In this paper, we tested the techniques developed by Murphy et al. (2011), Calzetti et al. (2010) and Rieke et al. (2009) to infer the SFR from the infrared flux. However, there exist a vast variety of similar techniques & calibrations (c. f. Pannella et al. 2015; Leroy et al. 2013, 2012, 2008; Wuyts et al. 2011).

[2] The top-hat function is not symmetric and evaluates at every point the average over the last 100 Myr.

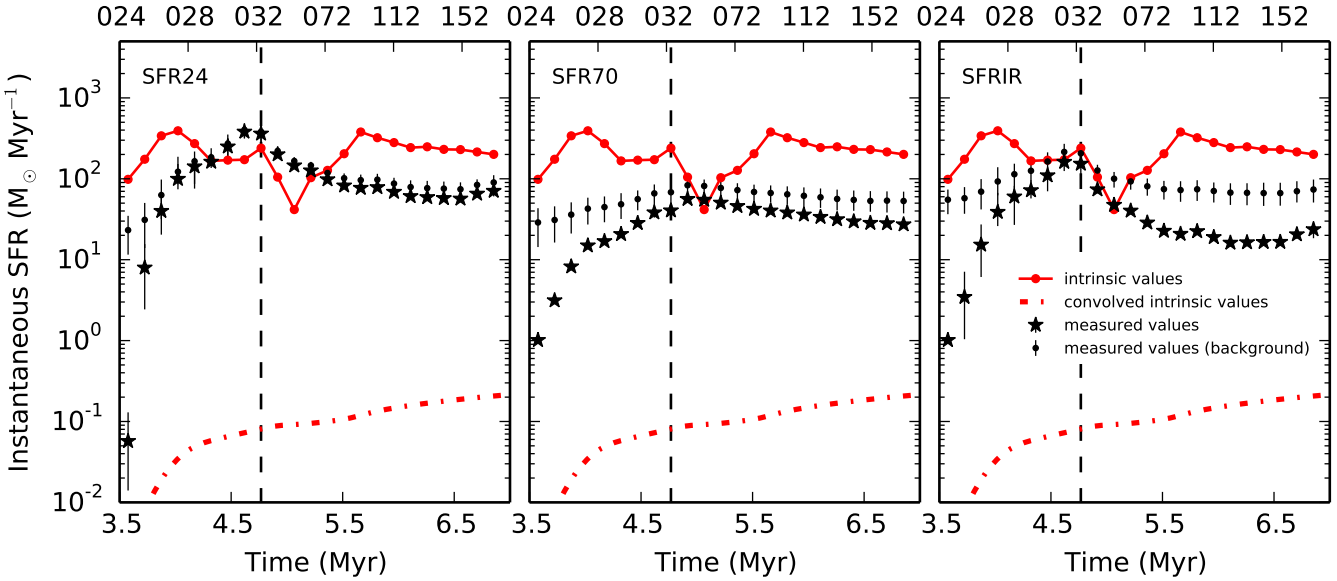

FIG. 1.— Averaged measured SFRs with the techniques SFR24, SFR70 and SFRIR using the total flux at 24 µm, 70 µm and the total infrared flux, respectively, in comparison with the intrinsic SFR.

from the simulation averaged over a similar timescale $\hat{\mathrm{SFR}}_{\mathrm{sim}}(\delta t_* = 100\,\mathrm{Myr})$. However, they should match if the technique worked accurately. We provide the measured values in Table 1 of Appendix A.

2.2. *Method SFR70 — 70 µm Tracer*

Based on *Spitzer* data, Calzetti et al. (2010) empirically calibrated the SFR using the total luminosity in 70 µm above $\nu L_\nu(70\,\mu\mathrm{m}) \geq 1.4 \times 10^{42}\,\mathrm{ergs\,s^{-1}}$:

$$\frac{\mathrm{SFR}_{70\,\mu\mathrm{m}}(\delta t_* = 100\,\mathrm{Myr})}{M_\odot\,\mathrm{yr}^{-1}} = 5.88 \times 10^{-44} \times \frac{\nu L_\nu(70\,\mu\mathrm{m})}{\mathrm{ergs\,s^{-1}}}. \quad (6)$$

Note that here we will use PACS 70 µm to estimate the $\mathrm{SFR}_{70\,\mu\mathrm{m}}(\delta t_* = 100\,\mathrm{Myr})$ with Eq. 6 and again test the SFR70 for luminosities below $10^{39}\,\mathrm{ergs\,s^{-1}}$. We show the results again in Figure 1 (black symbols in middle panel). We can see that the difference between the measurement with combined background (black dots) and the background-free measurements (black stars) is larger than for the method SFR24. This is again due to the high background of the Galactic plane (as explained in Paper II) and a result of the non-uniform background during background correction. Again, similarly to what we found for the SFR24 technique, the measured $\mathrm{SFR}_{70\,\mu\mathrm{m}}(\delta t_* = 100\,\mathrm{Myr})$ is two orders of magnitude higher than the expected value from the simulation $\hat{\mathrm{SFR}}_{\mathrm{sim}}(\delta t_* = 100\,\mathrm{Myr})$. We provide the measured values in Table 1 of Appendix A.

2.3. *Method SFRIR — Total Infrared Tracer*

Murphy et al. (2011) derived their star-formation relation from the STARBURST99 models (Leitherer et al. 1999) for the total infrared luminosity reaching from 8 µm to 1000 µm.

$$\frac{\mathrm{SFR}_{\mathrm{IR}}(\delta t_* = 100\,\mathrm{Myr})}{M_\odot\,\mathrm{yr}^{-1}} = 3.88 \times 10^{-44} \frac{L(\mathrm{IR})}{\mathrm{ergs\,s^{-1}}}. \quad (7)$$

We derive the total luminosity in the infrared under the assumption that our 7 bands from ν_0 (IRAC 8 µm) to ν_1 (SPIRE 500 µm) cover most of the infrared emission. We integrate (using Simpson's rule, see Bronstein et al. 2005, Press et al. 1992) to calculate the flux density $F_\nu^{\mathrm{corr}}(\lambda)$:

$$L(\mathrm{IR}) = \int_{\nu_0}^{\nu_1} d\nu F_\nu^{\mathrm{corr}}(\lambda) \quad (8)$$

With the total infrared luminosity $L(\mathrm{IR})$, we use Eq. 7 to derive the $\mathrm{SFR}_{\mathrm{IR}}(\delta t_* = 100\,\mathrm{Myr})$ for our set of synthetic observations. Again, in Figure 1 (right panel), we compare the measurements (black) with the values from the simulations (red). Again the measurements with combined background (black dots) are higher due to the complex background. The offset is comparable to the technique SFR70 because *Herschel* bands with high background have been used (see Paper II). For the background-free measurements (black stars), the simulation spread is again larger, which is due to the MIR parts of the total infrared flux (see SFR24 and SFR70). Overall, the technique SFRIR produces values of the $\mathrm{SFR}_{\mathrm{IR}}(\delta t_* = 100\,\mathrm{Myr})$ which are up to three orders of magnitude higher than the simulated rate $\hat{\mathrm{SFR}}_{\mathrm{sim}}(\delta t_* = 100\,\mathrm{Myr})$. We provide the measured values in Table 1 of Appendix A.

3. CHOOSING CHARACTERISTIC TIMESCALES

From the measured SFRs in Figure 1, we can see that the techniques above drastically over-predict the intrinsic SFR from the D14 SPH simulations when compared on the same timescale. However, as mentioned before, the techniques SFR24, SFR70 and SFRIR were designed for whole galaxies or large regions of galaxies where the star-formation sites are averaged out. The assumed characteristic timescales are longer, (e. g. $\delta t_* = 100\,\mathrm{Myr}$: Kennicutt & Evans 2012; Murphy et al. 2011; Calzetti et al. 2010; Rieke et al. 2009), since they are related to the lifetime of high-mass stars. For the "observed" star-forming

region presented in this work, the simulations stops after 7 Myr, which is assumed to be the time after the first supernova goes off. The supernova would suppress star formation within a timescale much shorter than 100 Myr and would cause the emission related to star formation to decay but to what extent remains unclear.

3.1. *Averaging over Large Scales*

We will now test whether we can obtain a better agreement between star-formation laws and our simulation, when considering star formation over longer timescales and on larger spatial scales. Currently, however, there exist no galactic simulations which cover enough dynamic range to recover the star-forming regions in the required detail. For now, we need to rely on the D14 SPH simulations. Therefore, to do this, we set up a toy model of a galaxy consisting of $N_{\rm clusters}$ star-forming regions at different evolutionary steps t.

We set the number of regions within the "galaxy" to $N_{\rm clusters} = 1.2 \times 10^5$ at different evolutionary steps randomly selected from the range $t \in [0, 100]$ Myr. We interpolate the luminosities $\nu L_\nu(24\,\mu\text{m})$, $\nu L_\nu(70\,\mu\text{m})$ and $L(\text{IR})$ for every region n and compute the sum of the different luminosities:

$$\nu L_\nu^{\rm galaxy}(24\,\mu\text{m}) = \sum_{n=0}^{N_{\rm clusters}} \nu L_{\nu,n}(24\,\mu\text{m}) \quad (9)$$

$$\nu L_\nu^{\rm galaxy}(70\,\mu\text{m}) = \sum_{n=0}^{N_{\rm clusters}} \nu L_{\nu,n}(70\,\mu\text{m}) \quad (10)$$

$$L^{\rm galaxy}(\text{IR}) = \sum_{n=0}^{N_{\rm clusters}} L_n(\text{IR}) \quad (11)$$

Since the simulation we use stops after 7 Myr, so we need to make assumptions about what happens to the emission after the end of the simulation, which corresponds to the time when the first supernova goes off. We consider two limiting cases:

1. **Sharp Stop**
   The supernova disrupts the region very quickly and the infrared emission is suppressed on a very short timescale.
2. **No Stop**
   We assume that the emission stays constant after the supernova has gone off, until 100 Myr.

If we assume that the emission stops sharply after the first supernova, we extract a lower limit on the total luminosity of:

$$\nu L_\nu^{\rm galaxy}(24\,\mu\text{m})\big|_{min} = 2.37 \times 10^{42}\,\text{ergs}\,\text{s}^{-1} \quad (12)$$

$$\nu L_\nu^{\rm galaxy}(70\,\mu\text{m})\big|_{min} = 2.16 \times 10^{42}\,\text{ergs}\,\text{s}^{-1} \quad (13)$$

$$L^{\rm galaxy}(\text{IR})\big|_{min} = 4.61 \times 10^{42}\,\text{ergs}\,\text{s}^{-1}. \quad (14)$$

However, if we assume that the emission will be constant after the first supernova, we recover an upper limit on the total luminosity of:

$$\nu L_\nu^{\rm galaxy}(24\,\mu\text{m})\big|_{max} = 4.13 \times 10^{43}\,\text{ergs}\,\text{s}^{-1} \quad (15)$$

$$\nu L_\nu^{\rm galaxy}(70\,\mu\text{m})\big|_{max} = 5.39 \times 10^{43}\,\text{ergs}\,\text{s}^{-1} \quad (16)$$

$$L^{\rm galaxy}(\text{IR})\big|_{max} = 7.28 \times 10^{43}\,\text{ergs}\,\text{s}^{-1}. \quad (17)$$

Note that the upper as well as lower limit of the total luminosity lie within the range of validity of the SFR24 and SFR70 techniques.

Following Section 2.1, Section 2.2 and Section 2.3, we calculate the rate $\text{SFR}_\lambda^{\rm galaxy}(\delta t_* = 100\,\text{Myr})$ of our toy "galaxy" for the lower limit of immediately suppressed emission after the supernova (case: sharp stop):

$$\text{SFR}_{24\,\mu\text{m}}^{\rm galaxy}(\delta t_* = 100\,\text{Myr})\big|_{min} = 0.48\,M_\odot\,\text{yr}^{-1} \quad (18)$$

$$\text{SFR}_{70\,\mu\text{m}}^{\rm galaxy}(\delta t_* = 100\,\text{Myr})\big|_{min} = 0.13\,M_\odot\,\text{yr}^{-1} \quad (19)$$

$$\text{SFR}_{\rm IR}^{\rm galaxy}(\delta t_* = 100\,\text{Myr})\big|_{min} = 0.18\,M_\odot\,\text{yr}^{-1}. \quad (20)$$

For the constant continuous emission after the first supernova (case: no stop) we calculate:

$$\text{SFR}_{24\,\mu\text{m}}^{\rm galaxy}(\delta t_* = 100\,\text{Myr})\big|_{max} = 8.38\,M_\odot\,\text{yr}^{-1} \quad (21)$$

$$\text{SFR}_{70\,\mu\text{m}}^{\rm galaxy}(\delta t_* = 100\,\text{Myr})\big|_{max} = 3.17\,M_\odot\,\text{yr}^{-1} \quad (22)$$

$$\text{SFR}_{\rm IR}^{\rm galaxy}(\delta t_* = 100\,\text{Myr})\big|_{max} = 2.83\,M_\odot\,\text{yr}^{-1}. \quad (23)$$

We now compute the intrinsic rate $\text{SFR}_{\rm sim}^{\rm galaxy}$ of our toy "galaxy". We can estimate the total stellar mass of the "galaxy" $M_*^{\rm galaxy}$ by summing over the simulated stellar mass $M_{*,n}$ of every star-forming region at their assigned age in the "galaxy":

$$M_*^{\rm galaxy} = \sum_{n=0}^{N_{\rm clusters}} M_{*,n}. \quad (24)$$

We found that $M_*^{\rm galaxy} = 8.40 \times 10^7\,M_\odot$ for the global timescale of $\delta t_* = 100$ Myr and therefore estimate the SFR averaged over 100 Myr to be:

$$\text{SFR}_{\rm sim}^{\rm galaxy}(\delta t_* = 100\,\text{Myr}) = \frac{M_*^{\rm galaxy}}{\delta t_*} = 0.84\,M_\odot\,\text{yr}^{-1} \quad (25)$$

We can compare the values of Eq. 18 to Eq. 23 with the actual rate of the "galaxy" $\text{SFR}_{\rm sim}^{\rm galaxy}(\delta t_* = 100\,\text{Myr})$ and find that the real value lies within the limits of the measurement from the SFR24, SFR70, and SFRIR techniques. The measurement from the SFR24 technique, with a sharp emission cut-off, lies closest to the actual value. This is interesting because MIPS 24 µm traces very recent emission, while the FIR includes dust emission unrelated to star formation.

Note that the wide width of the limits is due to our lack of knowledge of how fast and with what function the emission from the star-formation sites will decay after the first supernova goes off. Most likely the real value is close to the sharp drop in emission. Nevertheless, we would like to emphasize that the fact that the measurements lie within the regions does not prove that the techniques SFR24, SFR70 and SFRIR work on the global scales for which they have been designed for, but rather show that the reason that the methods do not work on a single region is because the emission from the region needs to be averaged over longer timescales. Further tests from small scales to large scales are needed to verify these methods.

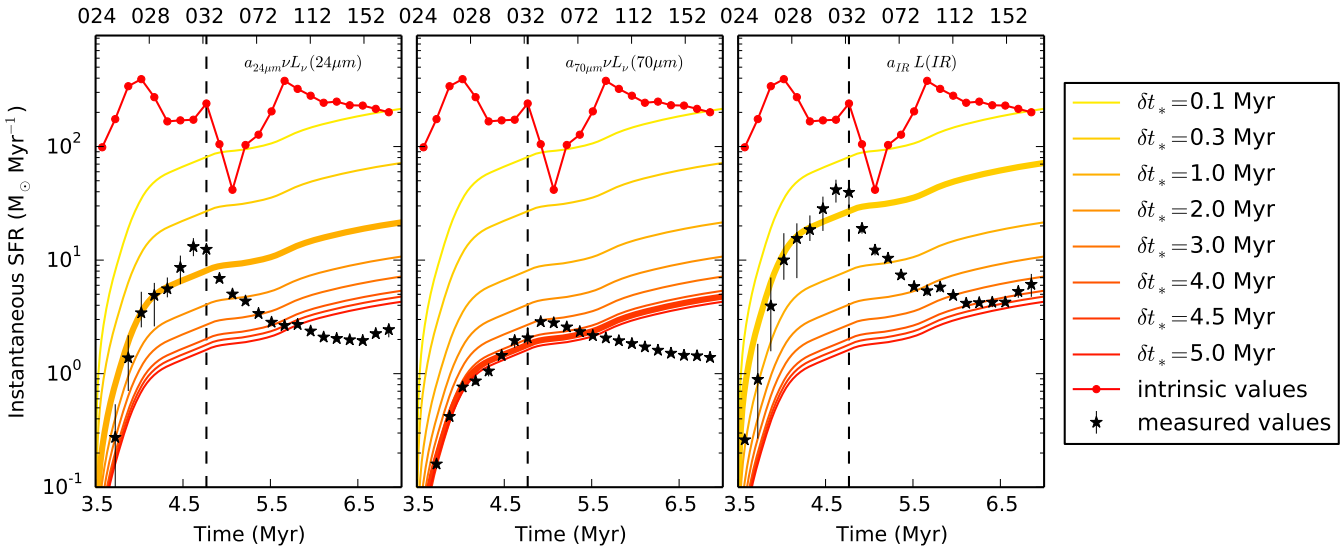

FIG. 2.— Instantaneous rate $\mathrm{SFR}_{\mathrm{sim}}(\delta t_* = \Delta t)$ from the simulation (red dots), rate convolved with different characteristic timescales δt_* (yellow to red) and the scaled measured emission (black stars). Numbers on top represent the time-step IDs and vertical lines highlight the time-step of the simulations when feedback was switched on.

3.2. *Calibration for Small Scales*

From Section 2.1 to Section 2.3, we showed that the measured values $\mathrm{SFR}_{24\,\mu\mathrm{m}}(\delta t_* = 100\,\mathrm{Myr})$, $\mathrm{SFR}_{70\,\mu\mathrm{m}}(\delta t_* = 100\,\mathrm{Myr})$ and $\mathrm{SFR}_{\mathrm{IR}}(\delta t_* = 100\,\mathrm{Myr})$ from the techniques SFR24, SFR70 and SFRIR, respectively, cannot reproduce the actual rate $\hat{\mathrm{SFR}}_{\mathrm{sim}}(\delta t_* = 100\,\mathrm{Myr})$ of the simulation on a size-scale of 30 pc. In Section 3.1, we showed however that for global scales which are governed by timescales of 100 Myr, the techniques work within the loose physical boundaries but require further investigation. In this section, we investigate whether the SFR24, SFR70 and SFRIR techniques could be improved for smaller scale star-forming regions.

In Figure 1, we saw a mismatch of the measured properties (black) and simulated properties (red). The difference is due to two effects:

1. The vertical scaling is off, which is due to the scaling factor a from Eq. 3. This factor needs to be adjusted when measuring on smaller scales.

2. The shape of the measured and simulated function differs. A difference of shape is due to a difference of timescale. On the scale of this individual region, the MIPS 24 µm emission appears to increase over 1 Myr before stabilizing due to the onset of high-mass stellar feedback.

In order to explore how we might achieve a better agreement, we again (see Bronstein et al. 2005; Press et al. 1992) convolve the intrinsic rate $\mathrm{SFR}_{\mathrm{sim}}(\delta t_* = \Delta t)$ with normalized top-hat functions of timescales δt_*, reaching from 0.1 Myr to 5.0 Myr, to reproduce the shape of the measured emission. We then vary the scaling factor a_λ for every measurement technique until a good fit between the convolved rate $\hat{\mathrm{SFR}}_{\mathrm{sim}}(\delta t_*)$, at the new timescale δt_*, and the measured emission is reached.

In Figure 2, we show the $\mathrm{SFR}_{\mathrm{sim}}(\delta t_* = \Delta t)$ (red dots) from the simulation and the convolved counterparts for different characteristic timescales δt_*. We highlighted the best fit of the convolved function $\hat{\mathrm{SFR}}_{\mathrm{sim}}(\delta t_*)$ and the scaled emission $a_{24\,\mu\mathrm{m}}\nu L_\nu(24\,\mu\mathrm{m})$, $a_{70\,\mu\mathrm{m}}\nu L_\nu(70\,\mu\mathrm{m})$ or $a_{\mathrm{IR}}\nu L(\mathrm{IR})$ as a thick line. Our fitted parameters for δt_* and a_λ are:

$$a_{24\,\mu\mathrm{m}} = 7 \times 10^{-45}\ \delta t_* \approx 1.0\,\mathrm{Myr} \quad (26)$$

$$a_{70\,\mu\mathrm{m}} = 3 \times 10^{-45}\ \delta t_* \approx 4.5\,\mathrm{Myr} \quad (27)$$

$$a_{\mathrm{IR}} = 1 \times 10^{-44}\ \delta t_* \approx 0.3\,\mathrm{Myr}. \quad (28)$$

Nevertheless, when inspecting Figure 2, one can see that it is challenging to pin-down a characteristic timescale, since for simulation time-steps where high-mass stellar feedback is present, the region is governed by different physical processes which also suppress the emission at later times.

4. EVOLUTION OF THE EMISSION

As noted in Section 3, we "observe" a drop in emission once the high-mass stellar feedback is switched-on. In Figure 3, we plot the evolution of the emission $\nu L_\nu(24\,\mu\mathrm{m})$, $\nu L_\nu(70\,\mu\mathrm{m})$ and the total infrared luminosity $L(\mathrm{IR})$ versus the stellar mass M_*. Since the points are equally spaced in time, we can see that the infrared emission increases steeply with increasing stellar mass in very few time-steps before (black) the stars start to ionize. Afterwards (red), the emission actually goes down with slightly increasing mass over many time-steps. We can see this evolution equally for the two monochromatic emissions in the MIR and FIR and also for the total infrared emission. We tried to quantify the change in emission of the two different episodes through a power-law fit of the following function:

$$\frac{L}{\mathrm{ergs\,s^{-1}}} = b \left(\frac{M_*^{\mathrm{sim}}}{M_\odot} \right)^c \quad (29)$$

We found from the "observed" set of synthetic observations that for regions where no high-mass stellar feedback is present, the emission versus stellar mass relation is represented very well by a power-law. The parameters for

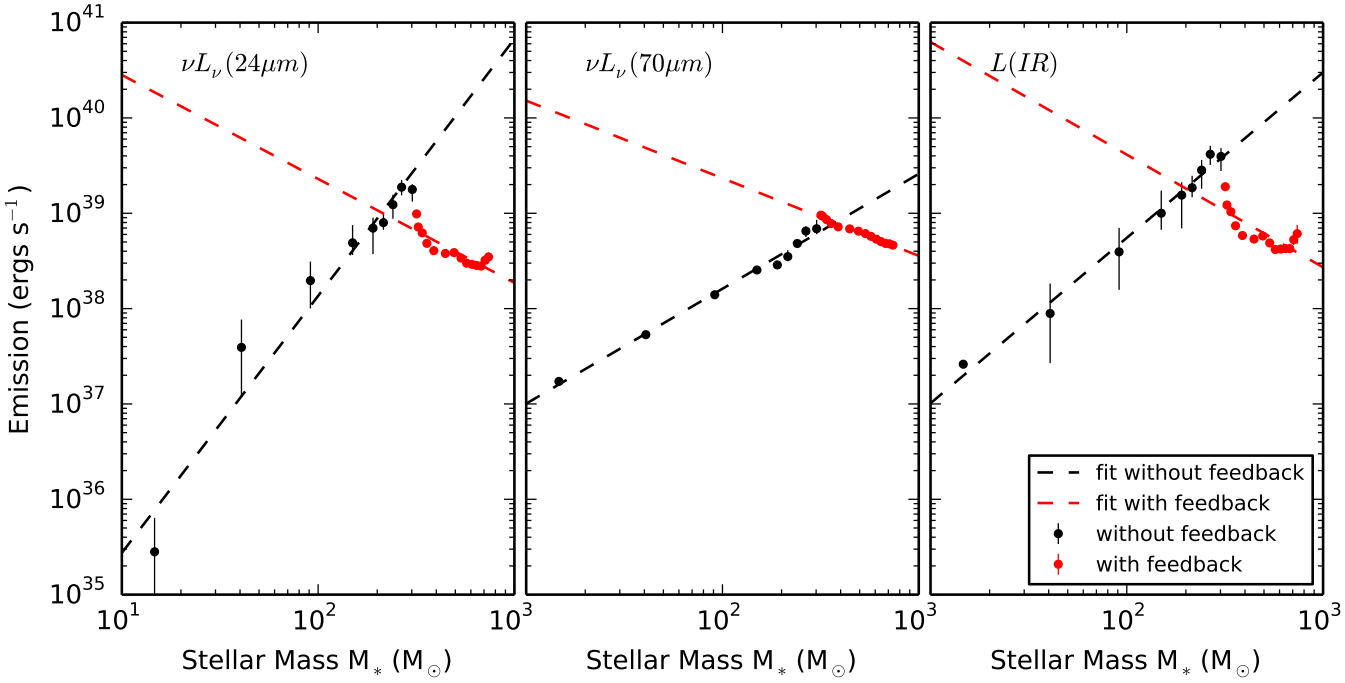

FIG. 3.— Relation of infrared emission and stellar mass in the simulated star-forming region; (black) time-steps without high-mass stellar feedback acting; (red) high-mass stellar feedback acts on region.

the different luminosities are:

$$b_{24\,\mu m} = 5.5 \times 10^{32} \quad c_{24\,\mu m} = 2.70 \tag{30}$$
$$b_{70\,\mu m} = 6.3 \times 10^{35} \quad c_{70\,\mu m} = 1.21 \tag{31}$$
$$b_{IR} = 1.9 \times 10^{35} \quad c_{IR} = 1.74. \tag{32}$$

When high-mass stellar feedback is present, the emission versus stellar mass relation also well fit by a power-law with the following fitting parameters:

$$b_{24\,\mu m} = 3.5 \times 10^{41} \quad c_{24\,\mu m} = -1.09 \tag{33}$$
$$b_{70\,\mu m} = 9.9 \times 10^{40} \quad c_{70\,\mu m} = -0.81 \tag{34}$$
$$b_{IR} = 9.5 \times 10^{41} \quad c_{IR} = -1.18. \tag{35}$$

These relations indeed show a very interesting development once the high-mass stellar feedback is acting in the star-forming region. The tilt in the power-law of the two different episodes can be explained through the ionizing bubble which is driven by the high-mass stellar feedback: Without high-mass stellar feedback most of the dust emitting in the MIR is located closer to the YSOs than the emission from the FIR. Once the stellar objects ionize and drive winds, the circumstellar material from this stars is eroded. Close-by accreting stars also lose their outer circumstellar material. Therefore, the turn-over of the power-laws is very rapid and cleaner for the 24 µm emission than for the 70 µm emission, as can be seen in Figure 3 (left & middle). Subsequently, the closer circumstellar material is eroded and the power-law in the Figure 3 tilts to negative values. The decreasing gas mass within the field of view also has an effect on the decreasing emission, however, this is not the dominating process. The same happens for the total infrared emission which is just a combination of the monochromatic 24 µm and 70 µm emission.

Note that even while high-mass stellar feedback is present in star-forming regions, star formation by itself does not stop completely. At the rim of the ionizing bubble, stars are still forming and growing.

5. PROTO-STELLAR COUNTING

We analyzed the point sources in our synthetic star-forming region and produced a point-source catalogue. In a follow-up paper (Paper IV), we will perform a detailed analysis regarding the SFR. Here, we concentrate on studying the point sources in the different circumstellar set-ups. In Figure 4, we present the number of point sources for the different time-steps and circumstellar set-ups.

In Section 4, we found that the number of accreting stars in the region is less than the number of young stars because some former accreting low-mass stars lost their material due to the high-mass stellar feedback of the neighboring stars. In Figure 4, the red dots represent the total number of stars (hence, ionizing stars, eroded YSOs and accreting YSOs), while the dashed line represents the number of accreting YSOs. We can see that the counted point sources (black stars) follow the trend of the accreting YSOs (dashed line). From Figure 4 (red dashed line), we can see that the number of accreting stars declines after the high-mass stellar feedback is switched on, but stabilizes again. The dip in the relation can be explained be cause the onset of high-mass stellar feedback redistributes star-formation in space and time.

The trend of the measured point sources is similar for the different circumstellar set-ups. However, we found that the set-up without circumstellar refinement (CM1) produced the brightest point sources. The brightness of forming stars with rotationally flattened envelope profiles (CM2) and with extrapolated power-law profiles (CM3) produces similar results. However, in some cases the accreting YSOs in CM3 remained undetected due to their very steep power-law profiles at the center of the en-

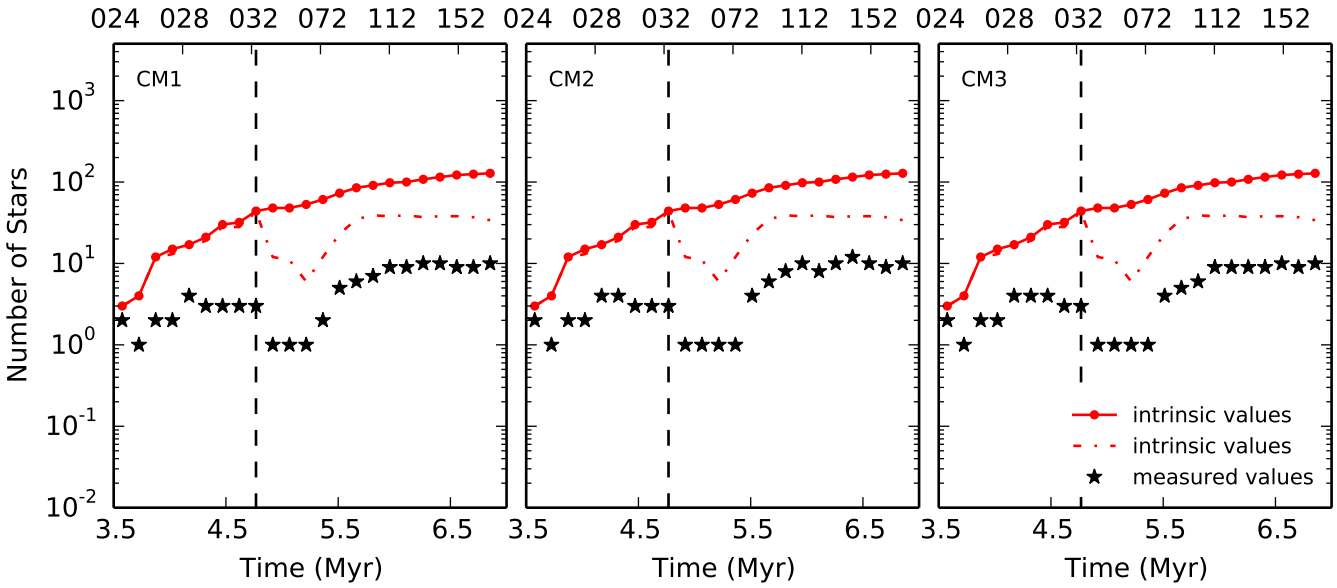

FIG. 4.— Counted number of stars for the different circumstellar set-ups (black) in comparison to the actual number of stars (red dots) and the actual number of accreting stars (dashed).

velopes.

Nevertheless, the number of accreting stars is about four times higher than the counted point sources, regardless the circumstellar set-up. This is mostly due to the detection limit in the synthetic star-forming region. In a follow-up paper (Paper IV), we will perform a population synthesis study to estimate the SFR directly from the young stellar population. The corresponding assumption of the IMF and the timescales will be studied in detail.

6. DISCUSSION

In the previous sections, we tested techniques commonly applied by observers to measure star-formation properties. We will now discuss the shortcomings and challenges when testing and measuring these properties:

6.1. *Choice of Diffuse Star-formation Tracers*

The SFR measurement techniques from Section 2 hold under the assumption that the infrared flux is solely due to the absorbed and re-emitted UV radiation from young high-mass stars. However, not all infrared emission, especially the FIR, is due to the channelling of UV photons. Hydrodynamical heating of the medium and the radiative heating of low-mass stars can also contribute to the flux. The feedback of low-mass young stars is important, since most of the stars are of low mass.

However, as stated before, the 24 µm emission mostly originates from star-formation sites and can act as a better proxy than the FIR. Techniques that make use of the total emission beyond 70 µm, such as SFR70 and SFRIR, are difficult to interpret, since they are simultaneously tracers of dust and gas (c. f. Paper II), rather than just tracers of sites of actual star formation and, therefore, the emission is also affected by the processes (e. g. high-mass stellar feedback) away from the individual star-formation sites (c. f. Section 4).

6.2. *Biases*

In what follows, we describe the biases introduced when measuring star-formation properties:

6.2.1. *Reliability of Local and Global Characteristic Time-scales*

When we observe local star formation on small scales, we probe regions that are governed by much shorter timescales, while for global scales (such as galaxies), variations of star formation happen over much longer timescales (Kruijssen & Longmore 2014). In Section 3, we explored the effect different timescales have on the recovered rates. We found that it is hard to single out one characteristic timescale which represents all the episodes of a star-forming region which are governed by different physics (e. g. early phases without feedback, high-mass stellar feedback, after first supernova).

Of course, these effects are averaged out when we observe galaxies, and one has to keep in mind that the recovered SFR is not the actual instantaneous SFR in the regions but just an average over the entire observation. In future, to test the accuracy of star-formation tracers on galaxy scales, one would of course ideally require a global simulation of a galaxy that also resolves individual forming stars.

6.2.2. *Reliability of the Measured Star-formation Rates*

In Section 2, we showed that empirical global diffuse star-formation tracers cannot be applied to local, small-scale regions. We showed examples of the calibration of SFRs for single star-forming regions by introducing new characteristic timescales and scaling factors. We note that for the small scales, where we probe the actual physics of star formation and where different processes act at different times (such as high-mass stellar feedback), it is difficult to single out one characteristic timescale and scaling factor for the entire star-forming region.

If our new relations to measure the SFR are used anyway, then we suggest the use of diffuse tracers only for regions at early stages, where ionization and winds are not present. From our synthetic observations combined with a background, we found that it is easiest to disen-

tangle the star-forming region at 24 µm from the background of the Galactic plane (compared to longer wavelengths). Therefore, biases due to the complex background are minimized.

6.2.3. *Propagation of Biases*

We would like to note that since there are still large biases when measuring the SFR from diffuse tracers. Further, the extracted stellar masses of a region are also biased, since they are a product of the SFR and characteristic timescale δt_* which are both very uncertain. In (Paper II), we showed that the estimated total gas masses of an individual star-forming region using modified blackbody fitting can produce reliable results in moderate background regions. However, the from the technique independent systematic errors (e. g. distance estimates) bias the total gas mass. Naturally, the estimates for the SFE (Eq. 2) which is just a combination of the stellar mass and the total gas mass should therefore be treated with caution.

6.3. *Impact of Feedback*

In Section 4, we showed that high-mass stellar feedback (ionization & winds) have a strong effect on the emission of the cloud in the infrared. The growing ionization bubble removes circumstellar material around the high-mass stars, which can be first observed at MIR wavelengths and then at later time-steps for FIR emission. The circumstellar envelopes of low-mass accreting stars are also eroded from the outside.

The simulations of D14 could be used further to explore the different feedback mechanisms on the synthetic observations, since they extensively modeled different combinations of ionization and winds. A finer grid of time-steps would be preferable to study the timescale under which the different feedback scenarios affect the emission in the different bands. Furthermore, simulations which include feedback physics on earlier time-steps in the simulation would be preferable. Currently in the D14, high-mass stellar feedback is switched on only after three stars have reached or exceeded the stellar mass of 20 $M_\odot$ and their accretion is suppressed. However, in reality, high-mass stars will ionize their surrounding in a continuous process while growing mass and the ionization processes is not "switched on" in a sharp manner.

6.4. *Tracer for Stellar Mass*

We found that on small scales, the infrared emission is a much better tracer of stellar mass M_* than of the SFR.

6.4.1. *Early Phases*

At early times in the simulations, where there is no high-mass stellar feedback present, we showed (see Section 4) that it is possible to define a simple relation $\frac{L}{\mathrm{ergs\,s^{-1}}} = b\left(\frac{M_*}{M_\odot}\right)^c$ between the infrared luminosities (at 24 µm, 70 µm or total infrared) and the stellar mass M_* of the region. We suggest using 24 µm emission to relate to the total stellar mass M_* in the star-forming region because the background is less complex in the MIR and the flux can be corrected more easily. Of course, this relation needs to be tested using other simulations before it can be generalized into a law that can be used on observed star-forming regions.

6.4.2. *High-Mass Stellar Feedback Phases*

Once the high-mass feedback is turned on, the infrared emission decreases, because the infrared emission is also a tracer of the dust. Changes in the geometry of the region, due to the high-mass stellar feedback, for example, pushing the dust further from the stars or destroying it (Diaz-Miller et al. 1998; Mathews 1967), can result in a decrease in the infrared emission.

As a result, we recommend against using the infrared luminosity as an accurate tracer of star formation on small scales where high-mass stellar feedback, such as ionization and winds, dominate.

6.5. *Stellar Population*

Here, we will discuss shortcomings and advances when sampling the stellar population directly:

6.5.1. *Circumstellar Set-up*

In Paper I, we described different circumstellar set-ups. In this paper (referred to as Paper III), we explored the synthetic observations resulting from Paper I and we showed that the different set-ups do not affect the total flux of the region at 24 µm much. However, the detectability of the point sources is dependent on the different types of inward extrapolation of the envelope profile.

We can see that numbers of measured point sources are similar for the different circumstellar set-ups. However, we found that the set-up without circumstellar refinement (CM1), produces the brightest point sources. The brightening for the objects without envelopes is due to the larger volume of dust exposed to the stellar radiation at the resolution radius of the simulation and also the larger stellar luminosity since the stellar mass was set to the mass of the sink particle in this case (see Koepferl et al. 2015 and Paper I for more details). The brightness of rotationally flattened profiles (CM2) and the extrapolated power-law profiles (CM3) produces similar results. However, in some cases the accreting YSOs with the CM3 set-up remained undetected due to their very steep power-law profiles at the center. When synthetic observations are used to study point sources, we therefore suggest using the rotationally flattened envelope profile to refine beyond the resolution radius, since it is consistent with the physical description of an infalling envelope. Nevertheless, we need to keep in mind that we deal here with low-number statistics.

6.5.2. *Initial Mass Function*

While the stellar mass is not biased due to characteristic timescales used when measuring the SFR through proto-stellar counting, the estimate of the total stellar mass is dependent on the assumption taken about the mass function of the stellar population. Especially, when we are limited in sensitivity. It is currently under debate whether the initial mass functions (e. g. Kroupa 2001; Salpeter 1955) hold for all local regions as well as on global scales (hence, in other galaxies) (see Offner et al. 2014). Jappsen et al. (2005) showed that the IMF depends on the thermodynamical state of the star-forming gas. However, the star-forming gas might vary at different locations, due to temperature, pressure, metallicity and chemistry in general. Therefore, it is challenging to

transfer the counted sample of YSOs to a reliable SFR. As an example, in the D14 simulations, during the time-steps where we see high-mass stellar feedback, and where we already have more than 100 stars, providing good number statistics, the simulation produces time-step dependent top heavy IMF. In the follow-up paper (Paper IV), we will explore the effects of the chosen IMF in more detail.

6.5.3. *Diffuse Star-formation Proxies versus Direct Counting*

In this paper (Paper III), we studied indirect diffuse star-formation tracers and showed that the commonly applied star-formation laws produce values that are too high when the techniques are applied to single star-forming regions (see Section 2). We showed that the techniques can be scaled in order to use them for single star-forming regions, even though the actual shape and pace of the instantaneous SFR is not recovered. However, when inspecting the detected point sources from our point-source catalogue (see Section 5), we found that the number of detected point sources follows the same trend as the number of accreting objects over time and is comparable to the instantaneous SFR.

7. SUMMARY

In this paper (Paper III), we explored different measurement techniques of star-formation properties such as the $\mathrm{SFR}_{24\,\mu\mathrm{m}}$, $\mathrm{SFR}_{70\,\mu\mathrm{m}}$, $\mathrm{SFR}_{\mathrm{IR}}$ and the gas mass M_{gas} from modified blackbody fitting for ∼5800 synthetic observations of a $\sim 30\,\mathrm{pc}$ star-forming region at different evolutionary time-steps, orientations, distances and different circumstellar radiative transfer set-ups. We further explored the accuracy of the techniques and the implications for small and for global scales:

- **Diffuse Monochromatic and Total Infrared Star-formation Tracers**
  On our synthetic star-forming region, we tested the diffuse monochromatic star-formation tracers of the total 24 µm and 70 µm emission originally designed for more global scales (Rieke et al. 2009 and Calzetti et al. 2010, respectively). Further, we explored the accuracy of the total infrared tracers (Murphy et al. 2011). We showed that these star-formation tracers deviate by several orders of magnitude from the intrinsic value. Further, we showed that in the FIR, it becomes more and more difficult to disentangle the synthetic region from the non-uniform background in the Galactic plane. We conclude that the star-formation tracers, using the diffuse infrared tracers developed for the extra-galactic community, do not work for our single star-forming region and hence, do not work on local scales, because we observe the peak of star formation and not its average, as this is the case for larger scales. Therefore, we suggest not to use these tracers as a star-formation proxy of single star-forming regions.

- **Characteristic Time-scales for Star-forming Regions**
  We explored which characteristic timescale relates the observed emission in the infrared with the actual star formation. We singled out timescales for regions not dominated by high-mass stellar feedback of 1.0 Myr, 4.5 Myr and 0.3 Myr for the 24 µm, 70 µm and the total infrared emission, respectively. We further adjusted the star-formation laws (see Eq. 3) for single star-forming regions, which do not yet experience high mass stellar feedback. We found scaling factors of 7×10^{-45}, 3×10^{-45} and 1×10^{-44} for the 24 µm, 70 µm and the total infrared emission, respectively. However, we suggest using the 24 µm star-formation tracer because it traces the direct sites of star formation and is not easily contaminated by Galactic emission (e. g. from the Galactic plane), which otherwise would lead to large biases.

- **Global Diffuse Star-formation Tracers**
  We further showed that for objects of larger scales, such as parts of galaxies, the diffuse star-formation tracers produce more consistent results. However, further tests, preferably with simulations with a larger dynamic range, are needed to verify the accuracy of the diffuse star-formation tracers on global scales and hence, for extra-galactic applications.

- **Impact of Feedback on the Emission**
  We found that high-mass stellar feedback affects the infrared emission almost instantly and produces a tip of the slope in the stellar mass versus infrared luminosity relation from positive to negative slopes. We found that since high-mass stellar feedback erodes the material first from inner regions of the YSOs, the emission at 24 µm is affected strongly compared to the 70 µm. Further tests with regions of different wind and different ionization power are needed to explore these effects further.

- **Tracer for Stellar Mass**
  We found that infrared emission is a much better tracer of stellar mass M_* than of the SFR on small scales and for phases without high-mass stellar feedback. We determine a power-law relation $\frac{L_{24\,\mu\mathrm{m}}}{\mathrm{ergs\,s^{-1}}} = 5.5 \times 10^{32} \left(\frac{M_*}{M_\odot}\right)^{2.70}$ between the 24 µm emission and the total stellar mass M_*. However, this relation breaks down once the stars start to ionize and drive winds.

- **Circumstellar Radiative Transfer Set-up**
  We explored the use of point sources at 24 µm to derive the SFR. While the different circumstellar set-ups do not affect the total flux at 24 µm much, the detectability of the point sources is dependent on the different types of inward extrapolation of the envelope profile. We found that the set-up without inwards extrapolation produces brighter point sources than the set-ups with the rotationally flattened and power-law envelopes. When synthetic observations are used to study point sources, we therefore suggest using the rotationally flattened envelope profile to refine beyond the resolution radius, since it is consistent with the physical description of an in-falling envelope.

- **Proto-stellar Counting**
  We explored the proto-stellar counting technique

at 24 µm and recovered a point-source catalogue for the different circumstellar set-ups. We showed that the trend of the detected point sources over time follows the trend of the number of accreted objects and hence the instantaneous SFR. In a follow-up paper (Paper IV), we will perform a detailed study of the recovered SFRs from proto-stellar counting.

We provide our measurements of the SFR from the different techniques and the measured gas mass in Table 1 of Appendix A. Moreover, the dust temperature and dust surface density maps will be provided in the online material of Appendix A.

8. ACKNOWLEDGEMENTS

We thank the referee for a constructive report that helped us improve the clarity and the strength of the results presented in our paper. This work was carried out in the Max Planck Research Group *Star formation throughout the Milky Way Galaxy* at the Max Planck Institute for Astronomy. C.K. is a fellow of the International Max Planck Research School for Astronomy and Cosmic Physics (IMPRS) at the University of Heidelberg, Germany and acknowledges support. C. K. acknowledges support from STFC grant ST/M001296/1. J. E. D. was supported by the DFG cluster of excellence *Origin and Structure of the Universe*. This research made use of Astropy, a community-developed core Python package for Astronomy (Astropy Collaboration et al. 2013), matplotlib, a Python plotting library (Hunter 2007), Scipy, an open source scientific computing tool (Jones et al. 2001–), the NumPy package (van der Walt et al. 2011) and IPython, an interactive Python application (Pérez & Granger 2007).

REFERENCES

Astropy Collaboration, Robitaille, T. P., Tollerud, E. J., et al. 2013, A&A, 558, A33
Barnes, A., Bally, J., Battersby, C., & Longmore, S. in preparation
Bate, M. R. 2009, MNRAS, 392, 590
—. 2014, MNRAS, 442, 285
Bronstein, I. N., Semendjajew, K. A., Musiol, G., & Mühlig, H. 2005, Taschenbuch der Mathematik, 6th edn. (Verlag Harri Deutsch)
Calzetti, D. 2013, Star Formation Rate Indicators, ed. J. Falcón-Barroso & J. H. Knapen (Cambridge University Press), 419
Calzetti, D., Wu, S.-Y., Hong, S., et al. 2010, ApJ, 714, 1256
Chomiuk, L., & Povich, M. S. 2011, AJ, 142, 197
Crocker, R. M., Jones, D. I., Aharonian, F., et al. 2011, MNRAS, 413, 763
Dale, J. E. 2015, New Astronomy Reviews, 68, 1
Dale, J. E., & Bonnell, I. 2011, MNRAS, 414, 321
Dale, J. E., Ercolano, B., & Bonnell, I. A. 2012, MNRAS, 424, 377
—. 2013a, MNRAS, 430, 234
Dale, J. E., Ngoumou, J., Ercolano, B., & Bonnell, I. A. 2013b, MNRAS, 436, 3430
—. 2014, MNRAS, 442, 694
Diaz-Miller, R. I., Franco, J., & Shore, S. N. 1998, ApJ, 501, 192
Draine, B. T. 2011, Physics of the Interstellar and Intergalactic Medium, 1st edn. (Princeton Universtiy Press)
Draine, B. T., & Li, A. 2007, ApJ, 657, 810
Evans, II, N. J., Dunham, M. M., Jørgensen, J. K., et al. 2009, ApJS, 181, 321
Federrath, C., Schrön, M., Banerjee, R., & Klessen, R. S. 2014, ApJ, 790, 128
Hansen, C. E., Klein, R. I., McKee, C. F., & Fisher, R. T. 2012, ApJ, 747, 22
Hunter, J. D. 2007, Computing In Science & Engineering, 9, 90
Jappsen, A.-K., Klessen, R. S., Larson, R. B., Li, Y., & Mac Low, M.-M. 2005, A&A, 435, 611
Jones, E., Oliphant, T., Peterson, P., et al. 2001–, SciPy: Open source scientific tools for Python, [Online; accessed 2012-2015]
Kennicutt, R. C., & Evans, N. J. 2012, ARA&A, 50, 531
Kim, S.-H., Martin, P. G., & Hendry, P. D. 1994, ApJ, 422, 164
Koepferl, C. M., & Robitaille, T. P. (in preparation, FluxCompensator Paper)
Koepferl, C. M., Robitaille, T. P., & Dale, J. E. 2016a, ApJ (accepted, Paper II)
—. 2016b, ApJ (accepted, Paper III)
Koepferl, C. M., Robitaille, T. P., Dale, J. E., & Biscani, F. 2016c, ApJS (accepted, Paper I)
Koepferl, C. M., Robitaille, T. P., Morales, E., & Dale, J. E. (in preparation, Paper IV)
Koepferl, C. M., Robitaille, T. P., Morales, E. F. E., & Johnston, K. G. 2015, ApJ, 799, 53
Kroupa, P. 2001, MNRAS, 322, 231
Kruijssen, J. M. D., & Longmore, S. N. 2014, MNRAS, 439, 3239
Krumholz, M. R., Klein, R. I., & McKee, C. F. 2011, ApJ, 740, 74
—. 2012, ApJ, 754, 71
Leitherer, C., Schaerer, D., Goldader, J. D., et al. 1999, ApJS, 123, 3
Leroy, A. K., Walter, F., Brinks, E., et al. 2008, AJ, 136, 2782
Leroy, A. K., Bigiel, F., de Blok, W. J. G., et al. 2012, AJ, 144, 3
Leroy, A. K., Walter, F., Sandstrom, K., et al. 2013, AJ, 146, 19
Longmore, S. N., Bally, J., Testi, L., et al. 2013, MNRAS, 429, 987
Mathews, W. G. 1967, ApJ, 147, 965
Misiriotis, A., Xilouris, E. M., Papamastorakis, J., Boumis, P., & Goudis, C. D. 2006, A&A, 459, 113
Murphy, E. J., Condon, J. J., Schinnerer, E., et al. 2011, ApJ, 737, 67
Murray, N., & Rahman, M. 2010, ApJ, 709, 424
Offner, S. S. R., Clark, P. C., Hennebelle, P., et al. 2014, Protostars and Planets VI, 53
Panagia, N. 1973, AJ, 78, 929
Pannella, M., Elbaz, D., Daddi, E., et al. 2015, ApJ, 807, 141
Pérez, F., & Granger, B. 2007, Computing in Science Engineering, 9, 21
Press, W. H., Teukolsky, S. A., Vetterling, W. T., & Flannery, B. P. 1992, Numerical Recipes in FORTRAN. The Art of Scientific Computing, 2nd edn. (Cambridge University Press)
Rieke, G. H., Alonso-Herrero, A., Weiner, B. J., et al. 2009, ApJ, 692, 556
Robitaille, T. P. 2011, A&A, 536, A79
Robitaille, T. P., & Whitney, B. A. 2010, ApJ, 710, L11
Salpeter, E. E. 1955, ApJ, 121, 161
Steinacker, J., Baes, M., & Gordon, K. D. 2013, ARA&A, 51, 63
Ulrich, R. K. 1976, ApJ, 210, 377
Urban, A., Martel, H., & Evans, II, N. J. 2010, ApJ, 710, 1343
van der Walt, S., Colbert, S., & Varoquaux, G. 2011, Computing in Science Engineering, 13, 22
Wuyts, S., Förster Schreiber, N. M., Lutz, D., et al. 2011, ApJ, 738, 106
Yusef-Zadeh, F., Hewitt, J. W., Arendt, R. G., et al. 2009, ApJ, 702, 178

APPENDIX

ONLINE MATERIAL FOR THE ANALYSIS OF SYNTHETIC STAR-FORMING REGIONS

In this appendix, we list the measured and simulated star-formation rates for the different combinations of circumstellar set-ups (CM1: no refinement, CM2: refinement with rotationally flattened envelope, CM3: refinement with power-law envelope), orientations (O1: xy plane, O2: xz plane, O3: yz plane) and distances (D1: 3 kpc, D2: 10 kpc).

TABLE 1 Measured Star-formation Rates for different time-steps and setups

setup (IDs)	run (ID)	time (Myr)	$\hat{\mathrm{SFR}}_{\mathrm{sim}}^{\delta t_*=100\,\mathrm{Myr}}$ ($M_\odot\,\mathrm{yr}^{-1}$)	$\mathrm{SFR}_{24\,\mu\mathrm{m}}^{\mathrm{B1}}$ ($M_\odot\,\mathrm{yr}^{-1}$)	$\mathrm{SFR}_{24\,\mu\mathrm{m}}^{\mathrm{B2}}$ ($M_\odot\,\mathrm{yr}^{-1}$)	$\mathrm{SFR}_{70\,\mu\mathrm{m}}^{\mathrm{B1}}$ ($M_\odot\,\mathrm{yr}^{-1}$)	$\mathrm{SFR}_{70\,\mu\mathrm{m}}^{\mathrm{B2}}$ ($M_\odot\,\mathrm{yr}^{-1}$)	$\mathrm{SFR}_{\mathrm{IR}}^{\mathrm{B1}}$ ($M_\odot\,\mathrm{yr}^{-1}$)	$\mathrm{SFR}_{\mathrm{IR}}^{\mathrm{B2}}$ ($M_\odot\,\mathrm{yr}^{-1}$)
CM1O1D1	024	3.576	2.24×10^{-9}	2.51×10^{-8}	3.48×10^{-5}	1.01×10^{-6}	4.33×10^{-5}	1.00×10^{-6}	7.34×10^{-5}
CM1O1D1	025	3.725	8.08×10^{-9}	3.99×10^{-6}	3.87×10^{-5}	3.06×10^{-6}	4.53×10^{-5}	1.69×10^{-6}	7.40×10^{-5}
CM1O1D1	026	3.874	1.91×10^{-8}	3.13×10^{-5}	6.61×10^{-5}	8.00×10^{-6}	5.03×10^{-5}	1.15×10^{-5}	8.37×10^{-5}
CM1O1D1	027	4.023	3.47×10^{-8}	1.53×10^{-4}	1.87×10^{-4}	1.45×10^{-5}	5.68×10^{-5}	6.69×10^{-5}	1.39×10^{-4}
CM1O1D1	028	4.172	4.88×10^{-8}	8.15×10^{-5}	1.16×10^{-4}	1.57×10^{-5}	5.79×10^{-5}	3.08×10^{-5}	1.03×10^{-4}
CM1O1D1	029	4.321	5.80×10^{-8}	1.93×10^{-4}	2.27×10^{-4}	2.41×10^{-5}	6.64×10^{-5}	9.18×10^{-5}	1.63×10^{-4}
CM1O1D1	030	4.470	6.52×10^{-8}	2.70×10^{-4}	3.05×10^{-4}	2.80×10^{-5}	7.02×10^{-5}	1.32×10^{-4}	2.03×10^{-4}
CM1O1D1	031	4.619	7.25×10^{-8}	3.89×10^{-4}	4.23×10^{-4}	3.35×10^{-5}	7.58×10^{-5}	1.74×10^{-4}	2.46×10^{-4}
CM1O1D1	032	4.768	8.13×10^{-8}	3.96×10^{-4}	4.30×10^{-4}	3.67×10^{-5}	7.90×10^{-5}	1.83×10^{-4}	2.54×10^{-4}
...	...	...	...	...	...	...	...	...	...

The full table will be provided in the online material.